LETTERS
https://doi.org/10.1038/s41567-022-01724-7

nature physics

Interaction-driven breakdown of dynamical localization in a kicked quantum gas

Alec Cao[1], Roshan Sajjad[1], Hector Mas[1], Ethan Q. Simmons[1], Jeremy L. Tanlimco[1], Eber Nolasco-Martinez[1], Toshihiko Shimasaki[1], H. Esat Kondakci[1], Victor Galitski[2] and David M. Weld[1]✉

Quantum interference can limit energy absorption in a continually kicked system through a single-particle ergodicity-breaking mechanism known as dynamical localization[1,2]. The effect of many-body interactions on dynamically localized states, although important to a fundamental understanding of quantum decoherence, has remained unexplored despite more than two decades of experimental studies[3–5]. Here we report the experimental realization of a kicked quantum rotor ensemble with tunable interactions using a Bose–Einstein condensate in a pulsed optical lattice. We observe a clear breakdown of dynamical localization due to interactions, but the resulting dynamics do not restore classical chaotic behaviour, instead displaying sublinear anomalous diffusion. Moreover, echo-type time-reversal experiments establish the role of interactions in destroying reversibility. These results quantitatively elucidate the dynamical transition to many-body quantum chaos and advance our understanding of quantum anomalous diffusion, with implications on the protection of quantum information in interacting driven systems.

Ergodicity breaking in quantum matter and the relaxation dynamics of thermalizing phases are two aspects of a central question of non-equilibrium many-body physics: how and when do isolated quantum systems thermalize? A growing body of theoretical and experimental work suggests that ergodicity can be avoided or hindered by a variety of mechanisms, including many-body localization[6,7], quantum many-body scarring[8,9] and prethermalization[10–14]. Even without ergodicity breaking, the expected emergence of quantum chaos on the addition of interactions to driven systems is not well understood. For example, the anomalous diffusion commonly observed near the interface between localized and ergodic regimes remains largely unexplained[10,15]. A general predictive understanding of such phenomena remains an open challenge to theory and experiment.

The quantum kicked rotor (QKR) is a paradigmatic model of quantum chaos and ergodicity breaking[16]. Although strong, repeated kicking drives a classical rotor into chaotic diffusion[17], the corresponding quantum rotor stops absorbing energy after a finite time, signalling the onset of dynamical localization. Despite the complete absence of disorder, this phenomenon can be understood as a manifestation of Anderson localization in momentum space[1,2]. Dynamical localization in the QKR was experimentally observed for the first time with cold atoms[3], and atom-optics QKR implementations have since proved to be a fruitful platform for the studies of localization-related phenomena[4,5,18,19]. The impact of interactions on the quantum suppression of classical chaos has attracted intense theoretical interest. Although nonlinearity induced by a mean-field interaction is expected to disrupt dynamical localization, the resulting behaviour is not classical chaos but instead a regime of quantum anomalous diffusion with sublinear energy growth[20–22]. This subdiffusive behaviour is reminiscent of nonlinear wave propagation in disordered media[23,24], and has also been predicted in the thermodynamic limit of coupled QKR models[25]. In certain kicked integrable models, however, many-body dynamically localized phases have been recently suggested[26,27], offering a new path towards stable driven interacting quantum states. Despite this extensive theoretical groundwork on interaction-based effects, experimental studies on

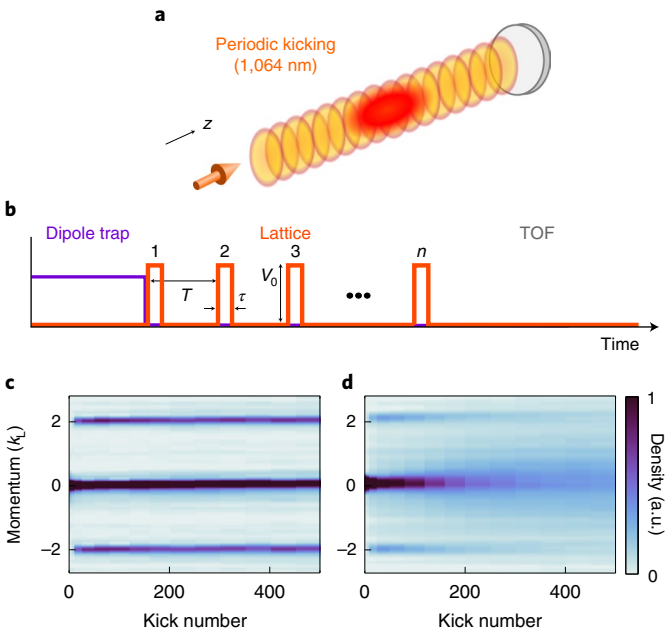

Fig. 1 | Experimentally realizing an interacting QKR. a, Schematic of a BEC in a single-pulsed optical lattice. **b**, Experimental sequence. After setting the scattering length, the trap is removed and kicking is applied with period T, pulse width τ and amplitude V_0 for n cycles. The atoms are imaged after TOF expansion. **c**,**d**, Measured axial momentum distribution versus kick number n for non-interacting ($0a_0$) (**c**) and interacting ($240a_0$) (**d**) samples kicked with parameters $V_0 = 64E_R$ and $T = 1.2\,\mu s$, revealing collisional momentum redistribution.

[1]Department of Physics, University of California, Santa Barbara, CA, USA. [2]Joint Quantum Institute and Condensed Matter Theory Center, University of Maryland, College Park, MD, USA. ✉e-mail: weld@physics.ucsb.edu

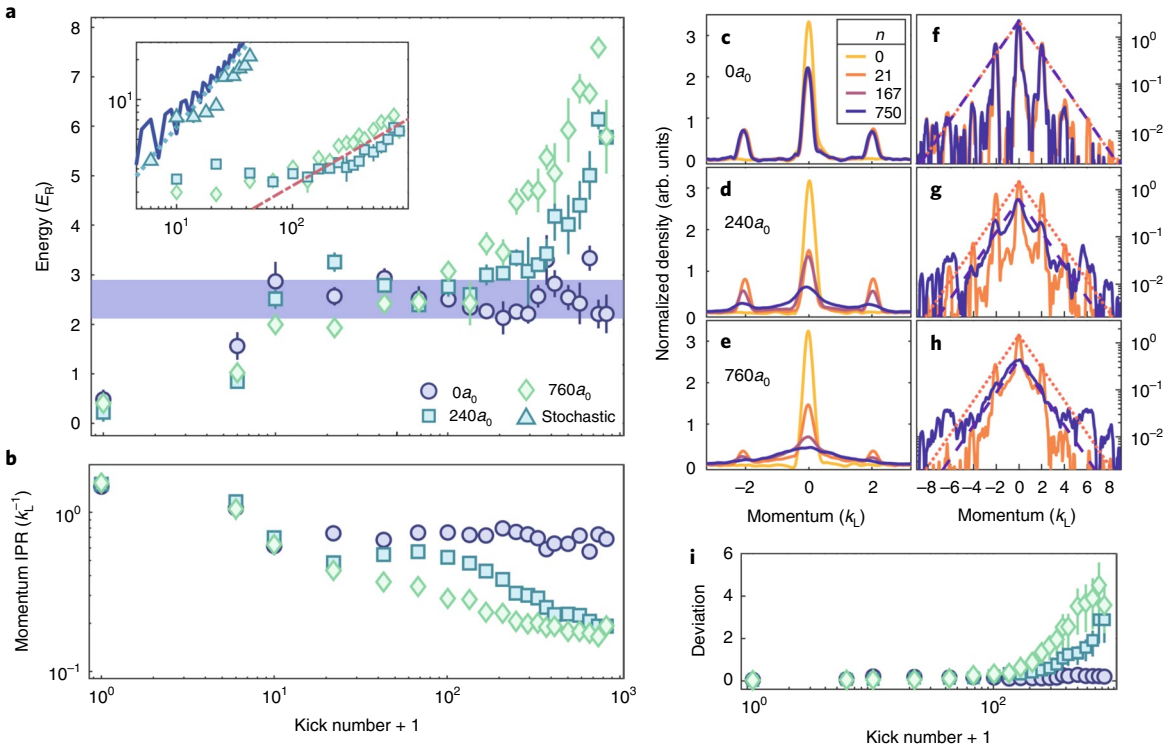

Fig. 2 | Observing the interaction-induced emergence of quantum chaos. a, Energy versus kick number for different scattering lengths a. The horizontal blue-shaded region indicates the measured single-rotor localization energy of $E_{loc} = 2.5(4)E_R$. Here $V_0 = 64E_R$, $T = 1.2\,\mu s$ and $\tau = 300\,ns$ ($K \approx 2.3$ and $\hbar \approx 1.5$). The inset contrasts the measured interaction-induced anomalous diffusion with classical-like diffusion caused by random kicking, the latter achieved by adding random offsets to the average kick spacing T drawn uniformly from the interval $[-T/4, T/4]$. The solid curve is non-interacting quantum theory and the dotted line is a diffusion curve $4Dn/\hbar^2$, where $D \approx 0.19$ is extracted from the classical standard map[17]. The red dot-dashed line is a subdiffusive $\sqrt{n}$ law serving as a guide to the eye. The error-bar computation is discussed in Methods. **b**, Evolution of effective 1D momentum-space IPR. **c**–**e**, Normalized momentum-space densities at various values of n. **f**–**h**, The same densities as in **c**–**e** but on a logarithmic y scale. The orange dotted and purple dashed lines are exponentially localized curves, namely, $\sim\exp(-k/k_{loc})$, where $k_{loc} = 1.2(1)k_L$ and amplitude normalized to match the peak of the measured distributions at the given kick number. **i**, Deviation from exponential localization over time based on the integrated ratio between the measured and exponential distributions with error bars computed from uncertainty in k_{loc}.

the robustness of dynamical localization have primarily focused on decoherence and noise;[28,29] beyond the single-rotor regime, only a single realization of two coupled kicked rotors has been presented, reporting a transition to classical diffusion[30]. Up to this point, experiments investigating dynamical localization in a truly many-body setting have remained unrealized.

Here we report the first experimental study of dynamical localization in the presence of tunable interactions. These experiments use a ^{7}Li Bose–Einstein condensate (BEC) kicked n times at period T by a far-detuned optical lattice of spacing $d = 532\,nm$ and depth V_0 for kick duration τ; the atoms undergo free propagation during the time between successive kicks (Fig. 1). Interactions are varied by tuning the s-wave scattering length a, reported in units of Bohr radius a_0, near a magnetic Feshbach resonance. The momentum distribution is imaged after time of flight (TOF). We report momentum and energy in units of $k_L = \pi/d$ and $E_R = \hbar^2 k_L^2/2m$, respectively, where m is the mass of ^{7}Li.

For $a \approx 0a_0$, our system maps to the single-particle QKR defined by the one-cycle Floquet map $U = e^{-i\hbar k^2/2} e^{-iK\cos(z)/\hbar}$ describing a cosine lattice impulse followed by free evolution. Here k and z are momentum and position, respectively; $K = \hbar V_0 \tau/2\hbar$ is the stochasticity parameter characterizing the kicking strength; $\hbar = 8E_R T/\hbar$ is the effective Planck constant determined by the kick period; and $\hbar$ is the reduced Planck constant. The dynamics are best visualized by considering a momentum-space lattice, with hopping induced by the kicks and onsite energy provided by the kinetic term. For generic $\hbar$ not tuned to a quantum resonance, these onsite energies form a pseudo-random sequence due to quadratic dispersion[2], yielding dynamical localization to a finite energy after a short diffusion time. As expected (Fig. 2a), we observe a rapid saturation in kinetic energy for the non-interacting condensate that persists for over 800 kicks.

In contrast, interacting samples with non-zero a (Fig. 2a) clearly demonstrate an interaction-induced breakdown of dynamical localization. At intermediate interaction strength ($a = 240a_0$), we observe initial saturation to the same energy as the non-interacting samples, followed by the onset of delocalization and sharp energy growth around 300 kicks. A more strongly interacting sample ($a = 760a_0$) exceeds this localized energy after 100 kicks, and does not obviously establish any quasi-equilibrium dynamical state. Figure 2b shows another aspect of the same evolution, plotting an effective one-dimensional (1D) momentum-space inverse participation ratio (IPR) versus kick number. The IPR value is a standard localization metric that characterizes the number of states over which a wavefunction is distributed (Methods provides additional discussion). Although the $240a_0$ data appear to exhibit an initial quasi-steady-state behaviour before delocalizing, the $760a_0$ IPR decreases monotonically for almost the entire experiment. Although the separation of timescales in the measured evolution of the $240a_0$ sample is suggestive of a prethermalization mechanism, further experiments are needed to better determine the nature of the intermediate-time state. In both IPR and energy measurements,

the main experimental result of this work is clear: interactions induce a breakdown of dynamical localization.

A second key result of these measurements is that the observed delocalizing dynamics clearly exhibit anomalous diffusion: it appears that even interacting QKRs absorb energy much more slowly than classical rotors. Figure 2a (inset) contrasts the nature of the observed interaction-induced subdiffusive delocalization with linear energy growth in the classically chaotic model. We experimentally simulate classical dynamics by adding stochastic fluctuations to the kicking period T, making use of the known sensitivity of dynamical localization to the timing noise[31]. These experimental data agree with both single-particle quantum numerics and linear energy growth predicted by the classical standard map[17], and stand in clear contrast to the measured interaction-induced anomalous diffusion away from the dynamically localized state. The red dot–dashed line (Fig. 2a, inset) indicates an $\sqrt{n}$ energy growth, and fitting the late-time data to n^{α} yields anomalous diffusion exponents α in the range of $[0.4, 0.6]$.

Does the observed anomalous diffusion agree with theoretical expectation? The most straightforward correction to the Floquet map U in the presence of interatomic interactions is the inclusion of a nonlinear mean-field term, which acts by non-locally coupling momentum sites between kicks. In this spirit, 1D Gross–Pitaevskii simulations on a ring have recently predicted a non-universal power law in the range of $\alpha \in [0.5, 0.8]$, overlapping with our observations[22]. However, it is not clear that mean-field theory should provide an accurate description of the experiments we report, even apart from the difference in dimensionality. The discrete momentum modes excited by the lattice feature a large momentum separation, leading to high-velocity interatomic collisions that elastically scatter atoms into a halo of unoccupied modes[32,33]. Due to the absence of a transverse confining potential, we indeed observe that these high-energy transverse momentum states become non-negligibly occupied during the interacting experiments, reliably indicating beyond-mean-field dynamics. Given the presence of violent collisional dynamics in the experiment, the approximate agreement of the observed subdiffusive exponent with 1D mean-field theory is interesting and rather surprising, and suggests the need for further exploration of the underlying mechanisms of anomalous diffusion in interacting QKR systems.

For further insights into the dynamics of kicked interacting quantum systems, we examine the evolution of momentum distribution (Fig. 2c–e). We observe a clear distinction between the non-interacting samples (which settle at a sharply peaked dynamically localized momentum distribution) and the interacting samples (which gradually smear out in momentum space over time). Plotting these same densities on a logarithmic scale (Fig. 2f–h) illuminates the destruction of dynamical Anderson localization by measuring the departure from exponential localization. Although the non-interacting distribution follows the expected exponential localization envelope for all times, the interacting distributions develop significant and growing population outside this envelope at late times. In Fig. 2i, we quantitatively characterize this growing deviation from exponential localization, revealing a break time near 200 kicks for both interaction strengths. Intriguingly, the smeared-out lower-energy modes of the $760a_0$ data appear to maintain the localization length long after the energy surpasses the localized value; instead, we find that the loss of exponential localization primarily manifests in the tails of the distribution. It is interesting to note that recent theory suggests that even many-body dynamically localized phases may exhibit universal power-law decaying tails[34]. These findings provide a second experimental signature of the destruction of the dynamically localized state by interactions, now both at the level of macroscopic observables and squared wavefunctions.

The onset of delocalization due to interactions indicates a transition to the regime of many-body quantum chaos, which

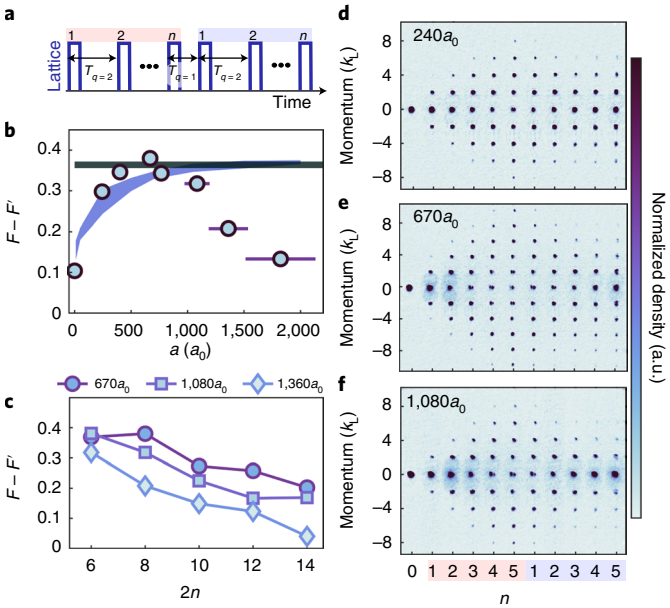

Fig. 3 | Effect of interactions on reversibility in echo experiments. **a**, Schematic of the time-reversal echo sequence with two trains of n pulses with period $T_{q=2} \approx 9.95\,\mu s$ separated by a wait time of $T_{q=1} \approx 4.98\,\mu s$. The first set of n kicks propagates the system forward in time and a second time-reversal set of n kicks propagates it backwards. **b**, Measured differential fidelity $F - F'$ for a range of scattering lengths $a = [0, 1800]a_0$ for $2n = 8$, where $2n$ indicates the total number of kicks. The circles show the experimental data. The blue-shaded curve shows the results of a non-interacting numerical simulation and the horizontal line shows the simulated asymptotic value of $F - F'$. The clear departure of the most strongly interacting points from this line is a signature of the interaction-driven destruction of reversibility. **c**, Measured differential fidelity $F - F'$ at three different interaction strengths as a function of total number of kicks $2n$ in a QKR echo experiment. **d**–**f**, Averaged absorption images of a BEC after the first n kicks of a $2n = 10$ echo protocol, for three different values of a. The vertical error bars in **b** and **c** represent the standard error. The error bar of the scattering length a represents the estimated systematic error in field-control electronics.

can be directly probed by studying time-reversal dynamics[35,36]. To this end, we probe the onset of chaotic dynamics by measuring the effect of interactions on a time-reversal protocol akin to a spin echo (Fig. 3a)[37,38]. The echo is realized using quantum resonances[39] that occur for $\hbar = 2\pi q$ (where q is rational); in particular, for $q = 2$ ($T \approx 9.95\,\mu s$), the free evolution in U largely vanishes and effective time reversal can be achieved by setting q to 1 for a single kick halfway through the sequence[37,38]. This procedure would create exact time reversal for a single zero-quasi-momentum state in the absence of interactions. Due to finite quasi-momentum spread and non-reversed interactions, the reversal is imperfect, yielding fidelity $F = \left|\langle\psi|U_2^{\dagger}U_1|\psi\rangle\right|^2$, where U_1 and U_2 are time-evolution operators differing by some perturbation. Because the scattering length affects the momentum width of the initial state and consequently the zero-mode population after n kicks ($F' = |\langle\psi|U_1|\psi\rangle|^2$), the quantity $F - F'$ is plotted (Fig. 3b,c) as a normalized measurement of the total return probability. Perhaps surprisingly, $F - F'$ initially increases as the scattering length a is turned up from zero. For weak interactions, U_1 and U_2 are primarily distinguished by the failure to reverse the sign of kinetic energy, and thus, the increase can be explained by the Thomas–Fermi reduction in the initial-state momentum spread. Eventually, for a roughly above $700a_0$, the interaction becomes the primary perturbation and $F - F'$ sharply decreases with a,

marking the transition to predominantly interaction-induced irreversibility. Non-interacting numerical calculations (Supplementary Information and Fig. 3b) support this interpretation, quantitatively predicting the initial increase in $F-F'$ but not the subsequent interaction-induced reduction in fidelity. This observation showcases the destruction in reversibility mediated by the presence of interactions during the kicking sequence. Note that due to the difference in kick period, the total time of the experiments shown (Fig. 3) is ~100 μs; therefore, the interaction effects become evident at similar timescales as those in Fig. 2. The decay in fidelity with the total number of kicks in an echo experiment is shown in Fig. 3b, and the images at different interaction strengths and kick numbers are shown in Fig. 3d–f. Figure 3c probes the dependence of $F-F'$ on kick number and interaction strength for a range of interactions where they are the primary cause of irreversibility. As expected from Fig. 3b, $F-F'$ decreases with both increasing a and $2n$. The use of echo techniques as a probe of many-body quantum chaos not only illuminates the origins of the delocalizing dynamics we observe but also opens up the intriguing possibility of extending these protocols to probe scrambling in many-body quantum chaotic systems[40].

In conclusion, we have experimentally realized a many-body ensemble of QKRs. Following the evolution of interacting samples over hundreds of kicks, we observe signatures of an initial transient steady state, followed by an interaction-induced breakdown of dynamical localization via anomalous diffusion, signalling the onset of many-body quantum chaos. The characterization of departure from the dynamically localized state indicates subdiffusive energy growth with an exponent near 0.5, easily distinguishable from classical Joule heating in a randomly kicked system, and reveals momentum-space distributions that are not exponentially localized. Measuring echo time-reversal dynamics with quantum resonance enabled us to directly probe the role of interaction-induced irreversibility in driving a transition to many-body quantum chaos. Together, these results demonstrate and quantitatively illuminate the emergence of interaction-driven quantum chaos in a paradigmatic localized system.

During the course of this experiment, we became aware of related efforts underway with another experimental group[41]. The availability of two independent experiments is very helpful in elucidating the physics of the interacting QKR, and the two experimental platforms are complementary. The other study utilizes a BEC of ^{174}Yb (an atom with nearly 25 times the mass of ^{7}Li) confined in a transverse two-dimensional optical lattice. Although there is no experimentally accessible Feshbach resonance in ^{174}Yb, interactions can be tuned via the atom number and transverse trap depth, and a 1D regime can be attained using the transverse lattice. In both experiments, many-body dynamical delocalization is observed when interactions are introduced, with a subdiffusive exponent near 0.5. We believe this agreement further strengthens the arguments presented in both papers.

Online content

Any methods, additional references, Nature Research reporting summaries, source data, extended data, supplementary information, acknowledgements, peer review information; details of author contributions and competing interests; and statements of data and code availability are available at https://doi.org/10.1038/s41567-022-01724-7.

Received: 6 October 2021; Accepted: 14 July 2022;
Published online: 26 September 2022

References

1. Fishman, S., Grempel, D. R. & Prange, R. E. Chaos, quantum recurrences, and Anderson localization. *Phys. Rev. Lett.* **49**, 509–512 (1982).
2. Grempel, D. R., Prange, R. E. & Fishman, S. Quantum dynamics of a nonintegrable system. *Phys. Rev. A* **29**, 1639–1647 (1984).
3. Moore, F. L., Robinson, J. C., Bharucha, C. F., Sundaram, B. & Raizen, M. G. Atom optics realization of the quantum δ-kicked rotor. *Phys. Rev. Lett.* **75**, 4598–4601 (1995).
4. Manai, I. et al. Experimental observation of two-dimensional Anderson localization with the atomic kicked rotor. *Phys. Rev. Lett.* **115**, 240603 (2015).
5. Chabé, J. et al. Experimental observation of the Anderson metal-insulator transition with atomic matter waves. *Phys. Rev. Lett.* **101**, 255702 (2008).
6. Nandkishore, R. & Huse, D. A. Many-body localization and thermalization in quantum statistical mechanics. *Annu. Rev. Condens. Matter Phys.* **6**, 15–38 (2015).
7. Abanin, D. A., Altman, E., Bloch, I. & Serbyn, M. Colloquium: many-body localization, thermalization, and entanglement. *Rev. Mod. Phys.* **91**, 021001 (2019).
8. Bernien, H. et al. Probing many-body dynamics on a 51-atom quantum simulator. *Nature* **551**, 579–584 (2017).
9. Serbyn, M., Abanin, D. A. & Papić, Z. Quantum many-body scars and weak breaking of ergodicity. *Nat. Phys.* **17**, 675–685 (2021).
10. Singh, K. et al. Quantifying and controlling prethermal nonergodicity in interacting Floquet matter. *Phys. Rev. X* **9**, 041021 (2019).
11. Rubio-Abadal, A. et al. Floquet prethermalization in a Bose-Hubbard system. *Phys. Rev. X* **10**, 021044 (2020).
12. Peng, P., Yin, C., Huang, X., Ramanathan, C. & Cappellaro, P. Floquet prethermalization in dipolar spin chains. *Nat. Phys.* **17**, 444–447 (2021).
13. Langen, T. et al. Experimental observation of a generalized Gibbs ensemble. *Science* **348**, 207–211 (2015).
14. Ueda, M. Quantum equilibration, thermalization and prethermalization in ultracold atoms. *Nat. Rev. Phys.* **2**, 669–681 (2020).
15. Weidinger, S. A. & Knap, M. Floquet prethermalization and regimes of heating in a periodically driven, interacting quantum system. *Sci. Rep.* **7**, 45382 (2017).
16. Haake, F., Gnutzmann, S. & Kuś, M. *Quantum Signatures of Chaos* (Springer, 2018).
17. Chirikov, B. V. A universal instability of many-dimensional oscillator systems. *Phys. Rep.* **52**, 263–379 (1979).
18. Lemarié, G., Lignier, H., Delande, D., Szriftgiser, P. & Garreau, J. C. Critical state of the Anderson transition: between a metal and an insulator. *Phys. Rev. Lett.* **105**, 090601 (2010).
19. Sajjad, R. et al. Observation of the quantum boomerang effect. *Phys. Rev. X* **12**, 011035 (2022).
20. Shepelyansky, D. L. Delocalization of quantum chaos by weak nonlinearity. *Phys. Rev. Lett.* **70**, 1787–1790 (1993).
21. Gligorić, G., Bodyfelt, J. D. & Flach, S. Interactions destroy dynamical localization with strong and weak chaos. *Europhys. Lett.* **96**, 30004 (2011).
22. Lellouch, S., Rançon, A., De Bïevre, S., Delande, D. & Garreau, J. C. Dynamics of the mean-field-interacting quantum kicked rotor. *Phys. Rev. A* **101**, 043624 (2020).
23. Pikovsky, A. S. & Shepelyansky, D. L. Destruction of Anderson localization by a weak nonlinearity. *Phys. Rev. Lett.* **100**, 094101 (2008).
24. Flach, S., Krimer, D. O. & Skokos, C. Universal spreading of wave packets in disordered nonlinear systems. *Phys. Rev. Lett.* **102**, 024101 (2009).
25. Notarnicola, S. et al. From localization to anomalous diffusion in the dynamics of coupled kicked rotors. *Phys. Rev. E* **97**, 022202 (2018).
26. Keser, A. C., Ganeshan, S., Refael, G. & Galitski, V. Dynamical many-body localization in an integrable model. *Phys. Rev. B* **94**, 085120 (2016).
27. Rylands, C., Rozenbaum, E. B., Galitski, V. & Konik, R. Many-body dynamical localization in a kicked Lieb-Liniger gas. *Phys. Rev. Lett.* **124**, 155302 (2020).
28. Ammann, H., Gray, R., Shvarchuck, I. & Christensen, N. Quantum delta-kicked rotor: experimental observation of decoherence. *Phys. Rev. Lett.* **80**, 4111–4115 (1998).
29. Klappauf, B. G., Oskay, W. H., Steck, D. A. & Raizen, M. G. Observation of noise and dissipation effects on dynamical localization. *Phys. Rev. Lett.* **81**, 1203–1206 (1998).
30. Gadway, B., Reeves, J., Krinner, L. & Schneble, D. Evidence for a quantum-to-classical transition in a pair of coupled quantum rotors. *Phys. Rev. Lett.* **110**, 190401 (2013).
31. Oskay, W. H., Steck, D. A. & Raizen, M. G. Timing noise effects on dynamical localization. *Chaos Soliton. Fract.* **16**, 409–416 (2003).
32. Norrie, A. A., Ballagh, R. J. & Gardiner, C. W. Quantum turbulence and correlations in Bose-Einstein condensate collisions. *Phys. Rev. A* **73**, 043617 (2006).
33. Deuar, P. & Drummond, P. D. Correlations in a BEC collision: first-principles quantum dynamics with 150,000 atoms. *Phys. Rev. Lett.* **98**, 120402 (2007).
34. Vuatelet, V. & Rançon, A. Effective thermalization of a many-body dynamically localized Bose gas. *Phys. Rev. A.* **104**, 043302 (2021).
35. Rozenbaum, E. B., Ganeshan, S. & Galitski, V. Lyapunov exponent and out-of-time-ordered correlator's growth rate in a chaotic system. *Phys. Rev. Lett.* **118**, 086801 (2017).

36. Gorin, T., Prosen, T., Seligman, T. H. & Žnidarič, M. Dynamics of Loschmidt echoes and fidelity decay. *Phys. Rep.* **435**, 33–156 (2006).
37. Ullah, A. & Hoogerland, M. D. Experimental observation of Loschmidt time reversal of a quantum chaotic system. *Phys. Rev. E* **83**, 046218 (2011).
38. Martin, J., Georgeot, B. & Shepelyansky, D. L. Cooling by time reversal of atomic matter waves. *Phys. Rev. Lett.* **100**, 044106 (2008).
39. Lepers, M., Zehnlé, V. & Garreau, J. C. Kicked-rotor quantum resonances in position space. *Phys. Rev. A* **77**, 043628 (2008).
40. Swingle, B., Bentsen, G., Schleier-Smith, M. & Hayden, P. Measuring the scrambling of quantum information. *Phys. Rev. A* **94**, 040302 (2016).
41. Toh, J. H. S. et al. Observation of many-body dynamical delocalization in a kicked ultracold gas. Preprint at http://128.84.4.18/abs/2106.13773 (2021).

Methods

Experimental platform and sequence. The experiments begin with a BEC of around 10^5 ^{7}Li atoms in a far-detuned optical dipole trap with trapping frequencies $\omega_{x,z}/2\pi \approx 40$ Hz and $\omega_y/2\pi \approx 56$ Hz, where z is the axis of optical lattice, y is the direction of gravity and x is the remaining orthogonal axis. The condensate is produced by optical evaporation at an s-wave scattering length of $a = 240a_0$, set by an applied magnetic field in the vicinity of the broad Feshbach resonance at 737 Gauss (ref. [42]). Immediately after evaporation, the fields are ramped to their desired value over 60–90 ms and maintained for the remainder of the experiment. The dipole trap is then extinguished and the BEC is repeatedly subjected to a pulsed 1D optical lattice with lattice constant $d = 532$ nm, laser wavevector $k_L = \pi/d$ and recoil energy $E_R = \hbar^2 k_L^2/2m$ (m is the mass of ^{7}Li). The full dynamics are then well described by the second-quantized Hamiltonian as

$$\begin{aligned}\mathcal{H} &= \int \mathrm{d}^3 r \hat{\Psi}^\dagger(\mathbf{r},t) H(\mathbf{r},t) \hat{\Psi}(\mathbf{r},t) \\ &\quad + \tfrac{g}{2} \int \mathrm{d}^3 r \hat{\Psi}^\dagger(\mathbf{r},t) \hat{\Psi}^\dagger(\mathbf{r},t) \hat{\Psi}(\mathbf{r},t) \hat{\Psi}(\mathbf{r},t)\end{aligned} \tag{1}$$

$$H(\mathbf{r},t) = \frac{p^2}{2m} + \frac{V_0}{2}\cos(2k_L z) I(x,y) \sum_n f_\tau(t - nT). \tag{2}$$

The key kick parameters are the lattice depth V_0, effective pulse width τ, and kick period T. Here V_0 is calibrated through a standard Kapitza–Dirac diffraction technique. Also, $f_\tau(t)$ denotes a unit-amplitude pulse function beginning at $t = 0$ of width τ. The experimental pulse is approximated by a piecewise function with a linear rise and fall of 200 ns duration before and after a plateau of variable hold time. For the experimental data in the main text with $\tau = 300$ ns between the half-maximum points, this hold duration is 100 ns. The scattering length a determines the two-body coupling coefficient $g = 4\pi\hbar^2 a/m$. Here $I(x,y)$ denotes the transverse intensity profile of the lattice beams normalized to unity maximum; this is approximately Gaussian as $I(x,y) \approx \mathrm{e}^{-2(x^2+y^2)/\sigma^2}$ with a measured $1/e^2$ beam radius of $\sigma \approx 65$ μm. The total duration of kicking is at most 1 ms for our longest experiments, significantly shorter than the 4 ms it takes the BEC to fall under the influence of gravity through the lattice beam waist.

To measure the momentum distribution, we perform absorption imaging of the atoms after free expansion. The TOF duration is 3.5 ms for the delocalization data and 2 ms for the echo data. Due to the low mass of ^{7}Li and the breadth of Feshbach resonance, coil inductance prevents sweeping the magnetic fields to the non-interacting regime for this expansion period. This means that additional scattering occurs during expansion, which may lead to systematic errors in the measured quantities (Supplementary Section 6). For the energy, we are able to account for this scattering in our analysis due to the energy-conserving nature of the collisions. For metrics such as IPR, such systematic errors are challenging to avoid. However, by tracking the evolution of these observables as a function of kick number at a fixed TOF duration, we can largely attribute the qualitative observed dynamics to the evolution under the Hamiltonian expressed in equation (1) as opposed to expansion. At large n, the majority of scattering happens during the kicking duration; therefore, expansion effects become negligible.

Delocalization data analysis. This section discusses the analysis behind the data in Fig. 2. Because the momentum distributions of the interacting samples significantly change over the course of the delocalization experiments, the quantities (Fig. 2) are directly computed from raw or averaged images as opposed to fitting procedures. However, this can make measurable quantities (such as energy) sensitive to noise, especially near the edge of the camera sensor due to quadratic weighting. To maximize the signal-to-noise ratio in our measurement, we analyse the raw images using an adaptive region of interest (ROI). First, a single-base ROI capturing all the detectable atoms at all times is created for each interaction strength. The integrated density in this ROI is used to post-select images with total atom numbers falling within a ±10% window of the mean to reduce variations in the interaction energy, which directly depends on the atom density. For these data, we take ten images at each kick number, of which typically four to seven images are discarded by this post-selection procedure. The ROI boundaries at each kick number are then determined by the points at which the cumulative summed distributions of the averaged image outwards from a centre point reach a threshold value. The thresholds are empirically set and the boundaries obtained by the following procedure. First, we compute the transverse bound by integrating out the entire axial direction to get the overall transverse distribution, find the point at which it crosses an 85% threshold and then expand the resulting boundary by a factor of 1.5 (1.2 in the delocalization data; Supplementary Section 1) to ensure all the atoms are captured. We then compute an axial boundary going point by point along the transverse direction; at each transverse point, we integrate over ten neighbouring transverse pixel rows to get a 'local' axial distribution, find the point at which it crosses a 99.8% threshold and expand by a factor 1.15. Finally, we smooth each ROI boundary and take a moving average across different kick numbers (four on each side). Crucially, we have confirmed that the qualitative observation of delocalization is not significantly altered from the simple case where we only use the initial single-base ROI across all the shots. However, the details of the trends should be more accurately captured by the adaptive procedure because the signal-to-noise ratio over the ROI is optimized at each kick number. All the measurable quantities are then calculated from the imaged densities within this region.

Since we do not observe any substantial atom loss during the kicking duration, we treat the imaged atomic densities as normalized distributions. For Fig. 2a,b, we compute the measured quantities from individual experimental runs and then average the results, with the reported error bar as the standard error of the mean. For Fig. 2i, we instead compute the averaged distributions first before computing the deviation from exponential localization; the error bars are computed from a Monte Carlo simulation of the uncertainty in k_{loc} discussed later. A smoothing filter is applied to the displayed densities (Fig. 2c–h) for visual clarity, but not in the subsequent calculation of the localization deviation (Fig. 2i).

To measure the energy, we compute the post-expansion spatial variance of the distribution in both kicking (z) and transverse (x) directions of the image. Assuming cylindrical symmetry, the kinetic energy is then calculated as $m(\langle z^2\rangle + 2\langle x^2\rangle)/2t_{TOF}^2$ with $t_{TOF} \approx 3.5$ ms (Supplementary Fig. 4). For an accurate measurement of the interacting samples, the inclusion of transverse energy is necessary to account for energy-conserving scattering processes that occur during both kicking and TOF. In addition, the inhomogeneous intensity profile of the beam $I(x,y)$ leads to a transverse energy oscillation in all the samples, including the non-interacting ones (Supplementary Section 5). Since we are not interested in this effect, we remove it to the leading order by subtracting off the non-interacting transverse energy from each trace such that the non-interacting energy is purely the kinetic energy along the kicking direction. To compute the error bars on the interacting data, we add the error of the total interacting energy and non-interacting transverse energy in quadrature. The single-particle localization energy E_{loc} is estimated by averaging the non-interacting trace for $n \geq 100$, and the reported uncertainty is based on the standard deviation of those points. We note that this uncertainty is not only due to experimental imperfections but also due to natural dynamical fluctuations, as evidenced by the results of non-interacting simulations like those shown in Supplementary Fig. 3.

We compute an effective 1D momentum-space IPR (Fig. 2b) by first integrating the imaged distributions along the transverse x dimension to obtain an axial density (Fig. 2c–h) and then summing the squares of this subsequent normalized axial density; mathematically, this operation is defined by $\int \left(\int\int |\psi(\mathbf{k})|^2 \mathrm{d}k_x \mathrm{d}k_y\right)^2 \mathrm{d}k_z$, where $\psi(\mathbf{k})$ is the three-dimensional momentum-space wavefunction; we note that one transverse integration is performed by the imaging process. We use this metric as a proxy for the full three-dimensional momentum-space IPR, defined by $\int |\psi(\mathbf{k})|^4 \mathrm{d}^3\mathbf{k}$. This avoids technical difficulties associated with reconstructing the full three-dimensional distribution $|\psi(\mathbf{k})|^2$ as well as enables simple comparisons to the IPR of 1D localized distributions.

In Fig. 2i, the plotted localization metric is $\int_{-k_0}^{k_0} \max[r(k) - 1, 0]\mathrm{d}k/2k_0$. Here $r(k) = |\psi(k)|^2/\exp(-k/k_{loc})$ is the ratio of the measured axial density (denoted as $|\psi(k)|^2$) and an exponential localization envelope. Here the maximum of $|\psi(k)|^2$ at each kick number is set to unity. For a continuous exponential distribution, the momentum-space localization length follows the relation $k_{loc}/k_L = \sqrt{(E_{loc}/2E_R)}$; for the reported results, we further take into account the discrete nature of the excited momentum modes. In this devised metric, taking the maximum of $r(k) - 1$ and 0 ensures that the result is only sensitive to the regions of distribution that decay more slowly than exponentially. That is, it interprets 0 as 'at least exponentially' localized with respect to a given localization length. However, we note that even a dynamically localized state occasionally exceeds an exponential envelope and thus yields a non-zero value for this metric; nevertheless, we find that a steadily increasing trend in this quantity over time provides an accurate indicator of departure from exponential localization for this system. The reported values and error bars are extracted by propagating a Gaussian uncertainty in the measured k_{loc} through a Monte Carlo simulation. We empirically fit the result to a log-normal distribution, with the reported markers and error bars (Fig. 2i) representing the mean and interquartile range of the fit. The Monte Carlo–simulated distributions are investigated in more detail in Supplementary Section 2.

Time-reversal experimental sequence and data analysis. Here we discuss the methods and analysis used to produce the data in Fig. 3. The echo experiments begin similarly to the previously described sequence; for a $2n$ kick sequence, the BEC is first kicked n times near quantum resonance at the parameters $V_0 \approx 50E_R$, $\tau = 300$ ns and $T = 9.95$ μs. For these data, we adjusted the lattice depth V_0 for different interaction strengths to achieve the same amount of absorbed energy after the first n kicks. This compensates for a decrease in energy absorption at the same lattice depth for higher interaction strengths, which we attribute to the increase in the Thomas–Fermi radius of the BEC relative to the lattice beam size. Neglecting this effect would artificially enhance the fidelity at very large interaction strengths due to a reduction in the effective stochasticity parameter K. We plot the zero-mode fraction after the first n kicks without time-reversal (denoted as F' Gauss; Supplementary Fig. 6) to benchmark this procedure to normalize the kicking amplitude.

After the first n kicks, we wait a half-period $T/2$ to spatially shift the wavefunction by half a lattice spacing, causing the sign of the subsequent kicks to be reversed. We then apply another sequence of n kicks using the same lattice parameters to complete the echo sequence (Fig. 3a). The time series (Fig. 3d–f) shows the absorption images averaged over five shots for each kick number n in a

$2n = 10$ experiment. Since we begin with a zero-momentum condensate mode, to measure the echo fidelity, we simply need to count the fraction of atoms remaining in this mode. Although atoms in other momentum modes coupled by the lattice are easily distinguished, atoms that have undergone scattering events into a smeared-out background distribution are not always well separated. Thus, to extract the return fraction, we fit the axial atomic distribution around the zero-momentum mode with a pair of Gaussians of varying widths. The narrower Gaussian accounts for atoms remaining in the zero-momentum condensate after expansion, whereas the broader Gaussian measures the atoms that have been collisionally ejected from the condensate[33,43]. In Fig. 3b, we show the fraction of atoms remaining in the narrow Gaussian and use this quantity as an estimate of echo fidelity. Scattering during expansion means that this necessarily underestimates the true fidelity, a possibility further addressed in Supplementary Section 6.

Non-interacting QKR numerics. One-dimensional simulations of the non-interacting kicked rotor problem for comparison with experimental data are executed in two ways. We either perform a split-step Fourier integration of the QKR Hamiltonian (equation (2)) to model the finite-width pulses or iterate the QKR Floquet map described in the main text. The simulations are typically performed with periodic boundary conditions over a single lattice site (except when modelling the TOF readout; Supplementary Section 4). We perform a Gaussian sampling of quasi-momenta with a standard deviation of $\sim 0.03 k_L$; for modelling the initial condition effects (Fig. 3), we adjust this parameter according to an effective momentum width associated with the Thomas–Fermi condensate radius that increases with a. Where appropriate, we additionally average over lattice depth to account for different parts of the sample experiencing a Gaussian distribution of beam intensities. For simulation of the stochastic kicking protocol, we use the same techniques and additionally average over 100 different realizations of fluctuations (note that this is slightly different than in the experiment where a single-kick-period disorder realization is used).

Data availability

All data needed to evaluate the conclusions in this study are presented in the Letter and the Supplementary Information.

Code availability

The codes used for data analysis and numerical simulation are available from the corresponding author upon reasonable request.

References

42. Pollack, S. E. et al. Extreme tunability of interactions in a ^{7}Li Bose-Einstein condensate. *Phys. Rev. Lett.* **102**, 090402 (2009).
43. Tenart, A. et al. Two-body collisions in the time-of-flight dynamics of lattice Bose superfluids. *Phys. Rev. Res.* **2**, 013017 (2020).

Acknowledgements

We acknowledge helpful conversations with A. Rançon, N. Yao and T. Schuster.
Funding: D.M.W. acknowledges support from the Air Force Office of Scientific Research (AFOSR FA9550-20-1-0240), the Army Research Office (ARO PECASE W911NF1410154) and the National Science Foundation (NSF CAREER 1555313 and QLCI OMA-2016245). D.M.W., R.S. and E.N.-M. acknowledge support from the UCSB NSF Quantum Foundry through the Q-AMASE-i program (grant no. DMR-1906325). V.G. was supported by US ARO contract no. W911NF1310172, NSF DMR-2037158 and the Simons Foundation.

Author contributions

A.C., R.S., H.M., E.Q.S., J.L.T., E.N.-M., T.S. and H.E.K. contributed to operate the experiment and perform the measurements. A.C., R.S. and H.M. analysed the data. A.C. conceptualized and performed the theoretical simulations of the rotor and spin models. V.G. and D.M.W. developed the idea for the experiment. D.M.W. supervised the work. A.C., R.S., H.M., V.G. and D.M.W. wrote the manuscript. All the authors contributed to the discussion and interpretation of the results.

Competing interests

The authors declare no competing interests.

Additional information

Supplementary information The online version contains supplementary material available at https://doi.org/10.1038/s41567-022-01724-7.

Correspondence and requests for materials should be addressed to David M. Weld.

Peer review information *Nature Physics* thanks Jakub Zakrzewski, Maarten Hoogerland and the other, anonymous, reviewer(s) for their contribution to the peer review of this work.

Reprints and permissions information is available at www.nature.com/reprints.